ChemComm

Check for updates

Heteroatom constructed covalent organic frameworks for oxygen electrocatalysis and rechargeable zinc–air batteries

Anup Kumar Pradhan, [ID] [a] Bhushan Kishor Nandre,[a] Pandiyan Sivasakthi,[a] Sayan Halder, [ID] [a] Sasanka Dalapati,[b] Asim Bhaumik, [ID] [c] Pralok K. Samanta*[a] and Chanchal Chakraborty [ID] *[a]

Two low-bandgap, metal-free donor–acceptor COFs exhibit bifunctional OER/ORR activity, with N,S-rich BTTh-TZ-COF delivering superior charge transport, abundant active sites, and enhanced solid-state ZAB performance.

Driven by fossil fuel depletion and associated environmental concerns, sustainable energy storage technologies such as rechargeable metal-air batteries (MABs) have attracted attention for their high theoretical energy density and eco-friendly nature. Here, the discharging and charging processes of the MABs are accompanied by the oxygen reduction reaction (ORR) and oxygen evolution reaction (OER) at the same electrode *via* multistep electron-transfer pathways.[1a] However, the ORR is intrinsically sluggish, mainly due to complex adsorption/desorption dynamics and a reaction pathway that involves multiple oxygen-containing intermediates, *e.g.*, OOH, O, and OH*. State-of-the-art ORR catalysts rely on Pt-based nanomaterials, but their high cost, scarcity, susceptibility to fuel crossover, and poor durability have driven the development of low-cost transition-metal alternatives for oxygen electrocatalysis and MABs.[1b–d]

Covalent organic frameworks (COFs), a class of porous crystalline polymers constructed from covalently linked building blocks, have recently emerged as versatile materials with a wide range of applications.[2] Guided by the reticular chemistry principles, COFs enable the construction of highly ordered networks in which moieties are precisely incorporated at the atomic scale. Additionally, the intrinsic physicochemical properties of COFs can be strategically tuned to achieve

electrocatalytic activity comparable to that of noble metals.[3] In this regard, very limited reports with heteroatom incorporated COFs like porphyrin-based COFs,[4] a cobalt-centered COFs,[5] quaternary phosphonium COFs with high hydroxide conductivity,[6a] and fluorinated COFs with enhanced oxygen-transport nanochannels[6b] are reported for high-performance ZABs. The heteroatom incorporation optimizes charge distribution and adsorption energies, enabling electrocatalytic activity comparable to that of conventional noble-metal-based catalysis.[7] Herein, we have reported two heteroatom-containing COFs [benzene-trithiophene (BTTh) and triazine-based **BTTh-TZ-COF**, triphenyl amine (TPA) and triazine-based **TPA-TZ-COF**] (Fig. 1a and b) for fabricating ZABs. The synthesis protocols of the COFs are given in the Electronic Supplementary Information (ESI),
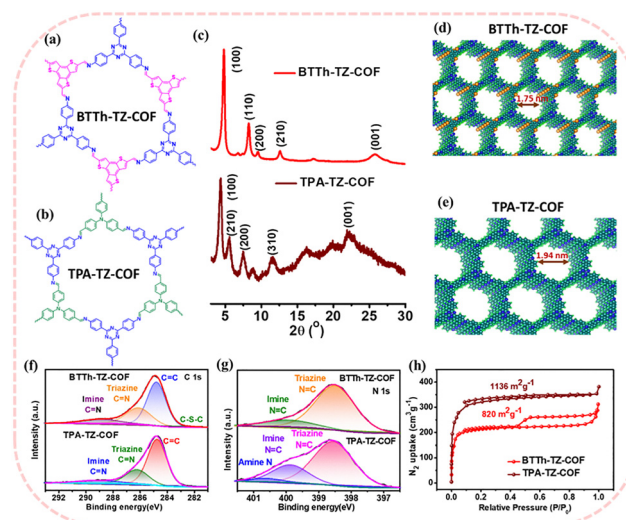

Fig. 1 Chemical structure of the (a) **BTTh-TZ-COF** and (b) **TPA-TZ-COF**. (c) Powder X-ray diffraction data of the COFs. The extended stacked structures of the (d) **BTTh-TZ-COF** and (e) **TPA-TZ-COF**, color codes: C – steel blue, H – green, S – orange, and N – blue. Core level XPS spectra of (f) C 1s and (g) N 1s, and (h) the BET-isotherm of the COFs.

[a] *Department of Chemistry, Birla Institute of Technology and Science, Pilani, Hyderabad Campus, Jawahar Nagar, Kapra Mandal, Medchal District, Telangana 500078, India. E-mail: pralokkumar.samanta@hyderabad.bits-pilani.ac.in, chanchal@hyderabad.bits-pilani.ac.in*

[b] *Department of Materials Science, School of Technology, Central University of Tamil Nadu (CUTN), Thiruvarur, 610005, Tamil Nadu, India*

[c] *School of Materials Sciences, Indian Association for the Cultivation of Science (IACS), 2A & 2B Raja S. C. Mallick Road, Jadavpur, Kolkata, 700032, West Bengal, India*

Scheme S1. **BTTh-TZ-COF** displays superior bifunctional electrocatalytic activity with a higher ORR onset potential (0.92 V vs. RHE) and lower OER overpotential (373 mV), and delivers higher specific capacity, energy, and power density in solid-state ZABs than **TPA-TZ-COF**.

The powder X-ray diffraction (PXRD) of the **BTTh-TZ-COF** and **TPA-TZ-COF** (Fig. 1c) confirms high crystallinity in both the COFs. The extended 2D COF models for both COFs, as shown in Fig. 1d-e, were built and optimized using density functional theory, as discussed in the SI. The XRD pattern of **BTTh-TZ-COF** shows diffraction peaks at $2\theta = 4.8°, 8.3°, 9.5°, 12.6°$, and $25.8°$ corresponding to the 100, 110, 200, 210, and 001 crystalline planes, respectively, and is consistent with previous reports.[8,9] In our previous report, the lattice dimensions of the hexagonal 2D **BTTh-TZ-COF** after Pawley refinement were reported as $a = b = 21.80$ Å, $c = 3.51$ Å, $\alpha = \beta = 90°$, and $\gamma = 120°$ with a profile residual (R_p) and weighted profile residual (R_{wp}) of 3.66% and 4.96%, respectively.[9] Similarly, **TPA-TZ-COF** crystallizes in a 2D hexagonal structure and shows diffraction peaks at 4.35°, 7.47°, 8.79°, 11.62°, and 24.10°, corresponding to the 100, 110, 200, 210, and 001 crystalline planes, respectively, as shown in Fig. 1c. The lattice dimensions of the **TPA-TZ-COF** are estimated to be $a = b = 22.58$ Å, $c = 3.62$ Å, $\alpha = \beta = 90°$, and $\gamma = 120°$ (Fig. S1 and Table S1 in the SI), whereas R_p and R_{wp} are 3.83% and 5.21%.

The elemental analysis of the COFs through XPS spectra reveals the presence of C, N, and S in **BTTh-TZ-COF**, and C and N in **TPA-TZ-COF**, as depicted in Fig. S2. As shown in Fig. 1f, the C 1s core level XPS spectra of **BTTh-TZ-COF** are fitted into four distinct peaks at 288.6, 286.3, 284.3, and 283.1 eV, attributed to C=N (imine), C=N (triazine), C=C (aromatic), and C–S–C bonds, respectively. The C 1s spectra of **TPA-TZ-COF** show three peaks at 284.5, 286.2, and 288.5 eV, corresponding to C=C (aromatic), N=C (triazine), and N=C (imine) carbon, respectively. The N 1s spectra of **BTTh-TZ-COF** are fitted into two peaks at 398.5 and 400.1 eV, corresponding to triazine N=C and imine N=C, respectively. Similarly, the N 1s spectra of **TPA-TZ-COF** show three fitted peaks of N=C (triazine), N=C (imine), and amine N at 398.6, 399.8, and 400.5 eV, respectively, as shown in Fig. 1g. Additionally, the S 2p spectra of **BTTh-TZ-COF** are fitted at 163.7 and 165.4 eV, corresponding to $2p_{3/2}$ and $2p_{1/2}$, as depicted in Fig. S3.

The Brunauer–Emmett–Teller (BET) surface areas of **BTTh-TZ-COF** and **TPA-TZ-COF**, measured through N_2 adsorption–desorption isotherms at 77 K, are estimated as 820 m^2 g^{-1} and 1136 m^2 g^{-1}, respectively. **BTTh-TZ-COF** exhibits a predominant type-I isotherm with a clear H1-type desorption hysteresis, whereas **TPA-TZ-COF** discloses a type-I isotherm with a sharp capillary N_2 uptake at low relative pressure ($P/P_0 < 0.04$) and gradual high-pressure adsorption, indicating coexisting micropores and mesopores arising from interparticle voids in the COFs.[10,11] The pore size distribution study shows the existence of 1D microporous channels within the 2D COF framework due to the π–π stacked layers, as shown in Fig. 1d and e. The total pore volumes and average pore sizes are calculated to be 0.25 cm^3 g^{-1} and 1.17 nm for **BTTh-TZ-COF**, and 1.18 nm for **TPA-TZ-COF**, with stretching up to 2 nm, well aligned with the theoretical pore sizes of 1.75 nm in **BTTh-TZ-COF** and 1.94 nm in **TPA-TZ-**

COF (Fig. 1d, e and Fig. S4 and Table S2), estimated from DFT-optimized structural models. The SEM study of **BTTh-TZ-COF** (Fig. S5) reveals a spherical aggregated morphology, whereas **TPA-TZ-COF** divulges the self-assembled aggregated structures. The substantial π–π stacking between the COF layers provides the highly aggregated morphologies in both cases. In the FT-IR spectra of **BTTh-TZ-COF** and **TPA-TZ-COF**, as shown in Fig. S6a and b, the characteristic C=O stretching frequencies at 1665 cm^{-1} and 1680 cm^{-1} attributed to the corresponding aldehyde precursors have disappeared in **BTTh-TZ-COF** and **TPA-TZ-COF**, respectively. The disappearance of the N–H stretching bands and the appearance of C=N stretching peaks at ~1581 and ~1588 cm^{-1} confirm complete precursor consumption and successful formation of imine-linked COF networks.

The solid-state UV-visible spectra (Fig. S7a) demonstrate **BTTh-TZ-COF** with a strong absorption at 468 nm with a broad NIR tail, while **TPA-TZ-COF** reveals a maximum at 394 nm with a shoulder at 472 nm, attributed to π–π* and n–π* transitions and donor–acceptor charge transfer within the frameworks.[12] The broader and more extended tail in **BTTh-TZ-COF** denotes the better donor–acceptor property in the BTTh-based donor than that of the TPA-based donor to the TZ-based acceptors in the framework. **BTTh-TZ-COF** exhibits a lower optical band gap (2.04 eV) than **TPA-TZ-COF** (2.31 eV) (Fig. S7b), consistent with the cyclic voltammetry (CV)-derived bandgap trend (Fig. S8, SI), indicating enhanced suitability of BTTh-TZ-COF for optoelectronic, electrical, and electrochemical applications. The HOMO and LUMO positions for **BTTh-TZ-COF** and **TPA-TZ-COF** are calculated to be −5.07 and −5.14 eV (HOMO) and −2.92 and −2.90 eV (LUMO), respectively.

Cyclic voltammograms of **BTTh-TZ-COF** and **TPA-TZ-COF** exhibit reduction peaks at 0.81 V and 0.78 V, respectively, in O_2-saturated 0.1 M KOH electrolyte (Fig. S9), confirming that the ORR on **BTTh-TZ-COF** is more thermodynamically favourable, as it occurs at a more positive potential.[13] Cathodic linear sweep voltammetry (CLSV) curves, as depicted in Fig. 2a, disclose a promising onset potential (E_{onset}) of 0.92 V and a half-wave potential ($E_{1/2}$) of 0.82 V for **BTTh-TZ-COF**. These values are much higher than those of the **TPA-TZ-COF**-based electrode ($E_{onset} = 0.83$ V and $E_{1/2} = 0.77$ V, Fig. 2b). Even the limiting current density of **BTTh-TZ-COF** (5.43 mA cm^{-2}) is higher than that of **TPA-TZ-COF** (4.56 mA cm^{-2}). Interestingly, the metal-free **BTTh-TZ-COF** reveals comparable ORR performance to a commercial 20% Pt/C catalyst ($E_{onset} = 1.01$ V, $E_{1/2} = 0.90$ V, and $J_L = 5.73$ mA cm^{-2}). Fig. 2a shows that, unlike Pt/C with a clear diffusion-limited plateau from fast 4e− ORR and high conductivity, **BTTh-TZ-COF** and **TPA-TZ-COF** exhibit continuously rising currents due to slower metal-free ORR kinetics and lower conductivity, indicating kinetic or mixed-control behaviour. Furthermore, the prepared **BTTh-TZ-COF** catalyst is more efficient in ORR activity than previously reported metal-free COF-based electrocatalysts, as depicted in Fig. 2b and Table S3. As shown in Fig. 2c, the **BTTh-TZ-COF** exhibits a lower Tafel slope (96 mV dec^{-1}) than the **TPA-TZ-COF** (124 mV dec^{-1}) and is comparable to Pt/C (87 mV dec^{-1}), indicating enhanced ORR kinetics in the **BTTh-TZ-COF**.[14] Consequently, the low Tafel slope of **BTTh-TZ-COF** also indicates a low oxygen coverage and
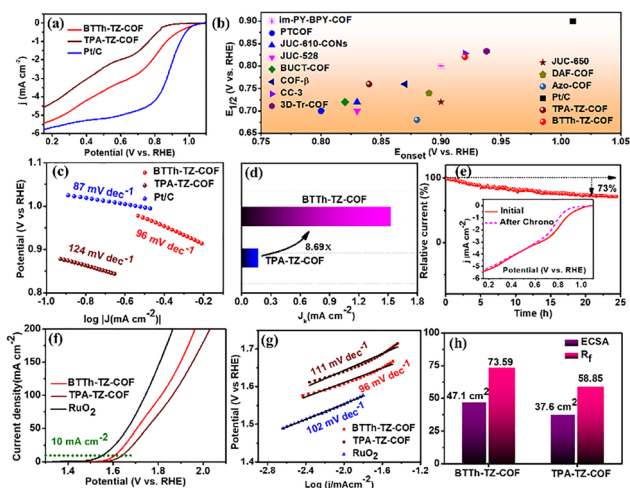
Fig. 2 (a) CLSV curves of different COFs and commercial Pt/C studied in O$_2$-saturated 0.1 M KOH solution at 1600 rpm. (b) Comparison plot of ORR metrics of the designed catalysts along with reported COF-based catalysts. (c) Tafel plots of catalysts interpreted from the CLSV curves at 1600 rpm. (d) Kinetic current density (J_k) of both the COFs. (e) Chronoamperometric stability test of **BTTh-TZ-COF** during the ORR. (f) ALSV curves and (g) corresponding Tafel plots of COFs and commercial catalyst in 1 M KOH. (h) ECSA and roughness factor (R_f) of both the COFs.

faster oxygen dissociation rate on the surface of **BTTh-TZ-COF** during ORR activity.[15] On the other hand, the kinetic current density (J_K) of **BTTh-TZ-COF** is 8.69 times higher than the J_K value of **TPA-TZ-COF** (Fig. 2d), implying the higher intrinsic ORR activity. The calculated number of transferred electrons during the ORR at 0.56 V using the Koutecky–Levich (K–L) equation is 3.24 and 2.89 for **BTTh-TZ-COF** and **TPA-TZ-COF**, respectively (Fig. S10a–c). These results indicate a more efficient dissociative pathway in **BTTh-TZ-COF** than in **TPA-TZ-COF**. Again, the **BTTh-TZ-COF** divulges high catalytic stability as it retains 73% relative current density even after 25 h (Fig. 2e). Anodic linear sweep voltammetry (ALSV) curves in Fig. 2f reveal that the **BTTh-TZ-COF** and **TPA-TZ-COF** require 52 mV and 90 mV more overpotential than that of commercial RuO$_2$ (321 mV). The corresponding Tafel slopes (**BTTh-TZ-COF**: 96 mV dec^{-1}, **TPA-TZ-COF**: 111 mV dec^{-1}, and RuO$_2$: 102 mV dec^{-1}) confirm the better charge transfer over the electrocatalytic interface in **BTTh-TZ-COF** catalysts with enhanced OER kinetics (Fig. 2g). Again, the better catalytic performance of **BTTh-TZ-COF** is attributed to its higher ECSA of 47.1 cm^2 and higher R_f of 73.59 than that of **TPA-TZ-COF** (ECSA: 37.6 cm^2, R_f: 58.85), as shown in Fig. S11 and Fig. 2h. The ECSA normalized LSV curves in Fig. S12 disclosed quite similar current density in **BTTh-TZ-COF** compared to **TPA-TZ-COF**, indicating that the enhanced catalytic activity of **BTTh-TZ-COF** primarily originated from the higher active site. Moreover, the post-OER XPS analysis of **BTTh-TZ-COF** and **TPA-TZ-COF**, as shown in Fig. S13, indicates that the C1s, N1s, and S2p spectra of both COFs remain largely unchanged compared to the pristine samples, indicating preservation of chemical environments and negligible structural reconstruction. The appearance of a broad peak around 292 eV in the C 1s spectra was attributed to the presence of –CF$_2$– in the sample, as Nafion was used as a binder.

The theoretical study based on the DFT method provides detailed information about the OER and ORR mechanisms for **BTTh-TZ-COF** and **TPA-TZ-COF** (Fig. 3a, b and Table S4 and Fig. S14–S18).

The rate-determining step for the OER is the *O to *OOH conversion, as it is the highest energy barrier for both **BTTh-TZ-COF** and **TPA-TZ-COF**. The overall lower energy reaction pathway for **BTTh-TZ-COF** makes **BTTh-TZ-COF** a more favourable catalyst for the OER and ORR than **TPA-TZ-COF** (Fig. 3a and b). The higher efficiency of **BTTh-TZ-COF** towards the OER and ORR is due to the favourable adsorption of different species (Tables S4 and S5). DFT analysis indicates that OH adsorption during the OER is dominated by the C1 site in **BTTh-TZ-COF**, while the C4 site is most active in **TPA-TZ-COF** (Fig. S14). The adsorption energies for OH$^-$ are 1.74 eV and 2.26 eV in **BTTh-TZ-COF** and **TPA-TZ-COF**, respectively. Although the energy barrier of *O to *OOH for **BTTh-TZ-COF** (2.79 eV) is higher than that of **TPA-TZ-COF** (2.51 eV), the presence of much higher density of active sites in **BTTh-TZ-COF** (6 and 3 active sites per unit in **BTTh-TZ-COF** and **TPA-TZ-COF**, respectively, Table S5) compensates for the higher barrier, resulting in a lower overpotential and better overall efficiency. Thus, the presence of S-containing donors in **BTTh-TZ-COF**, along with the N-containing moieties, generates better adsorption and higher active site density in the **BTTh-TZ-COF** framework than in the only N-containing **TPA-TZ-COF**. Again, the 4-electron transfer process is more favourable than the 2-electron process for the ORR of both COFs, consistent with our experimental data.

To meet the growing demand for energy, we fabricated a solid-state ZAB with COF on a Ni-foam air cathode, a Zn-plate anode, and a PVA–KOH–Zn(CH$_3$COO)$_2$ gel electrolyte.[16] The single-cell OCV values are 1.13 V for **BTTh-TZ-COF** and 1.07 V for **TPA-TZ-COF** (Fig. 4a). The **BTTh-TZ-COF**-based ZAB delivers a higher areal power density of 26.36 mW cm^{-2} at 28.15 mA cm^{-2} compared to 25.02 mW cm^{-2} at 15.57 mA cm^{-2} for **TPA-TZ-COF** (Fig. 4b), indicating superior charge transfer on the electrode surface of **BTTh-TZ-COF** during discharging. The significant discharge activity in the solid-state device primarily stems from the systematically enhanced ORR activity of **BTTh-TZ-COF**.

BTTh-TZ-COF and **TPA-TZ-COF**-based solid-state ZABs exhibit specific capacities of 23.84 and 21.38 mAh, respectively, at 2 mA cm^{-2} (Fig. 4c). Both ZABs show stable cycling over 30 h (Fig. 4d), with **BTTh-TZ-COF** achieving a higher round-trip efficiency (64%) than **TPA-TZ-COF** (60%) (Fig. 4e). EIS results
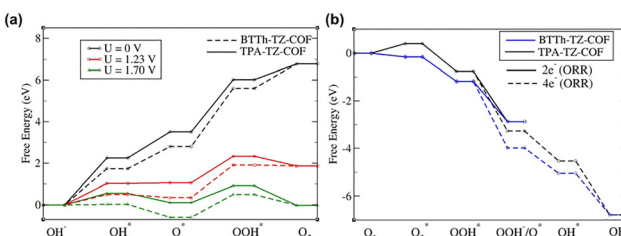

Fig. 3 Energy profile for the (a) OER and (b) ORR, on **BTTh-TZ-COF** and **TPA-TZ-COF** using the PBE exchange–correlation functional. U is the applied bias for the OER.
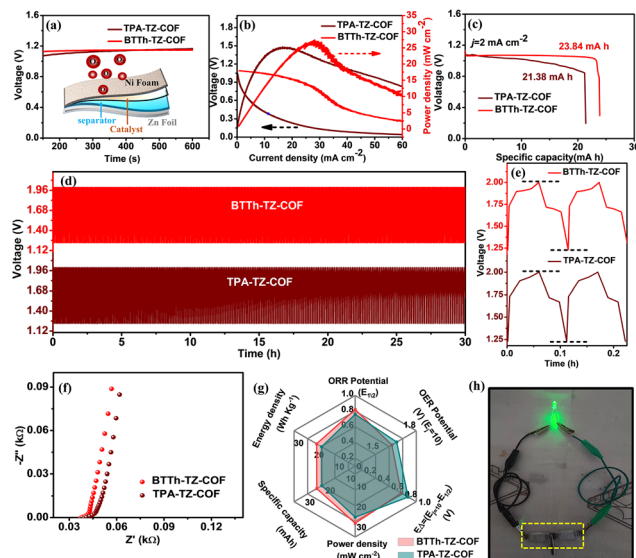
Fig. 4 (a) OCV of COF-based ZABs and schematic of a solid-state rechargeable ZAB. (c) Specific capacity at 2 mA cm⁻². (d) Long-term cycling stability. (e) Charge–discharge profiles for round-trip efficiency. (f) Nyquist plots. (g) Spider chart comparing **BTTh-TZ-COF** and **TPA-TZ-COF** performance. (h) Lighting a green LED with two ZABs in series.

(Fig. 4f) confirm low charge transfer resistance (R_{CT}) for both COFs; in particular, the R_{CT} of **BTTh-TZ-COF** is lower than that of **TPA-TZ-COF**. The spider chart (Fig. 4g) compares the overall electrochemical performances of **BTTh-TZ-COF** and **TPA-TZ-COF**, revealing better oxygen electrocatalysis in **BTTh-TZ-COF**. Two **BTTh-TZ-COF** containing ZABs connected in series can light up a green LED bulb (Fig. 4h), signifying the practical demonstration of the **BTTh-TZ-COF**-based ZAB. Moreover, the battery performances of our COF-based ZABs are compared with those of previously reported COF-based ZABs in Table S6.

In summary, two low-bandgap, metal-free, donor–acceptor porous COFs are prepared to compare their bifunctional OER and ORR electrocatalytic activities. The S-containing **BTTh-TZ-COF** exhibits better donor–acceptor properties, a lower bandgap, improved transport properties, higher ECSA, and more active sites, surpassing the OER or ORR activity of **TPA-TZ-COF**. DFT calculations also demonstrate a lower reaction energy barrier for bifunctional electrocatalysis in **BTTh-TZ-COF**. Furthermore, the solid-state ZAB constructed with BTTh-TZ-COF as the air cathode exhibits higher specific capacity, energy, and power densities than **BTTh-TZ-COF**. This work offers new insights into the design of catalytic donor–acceptor COFs for advanced energy storage and conversion applications.

Conflicts of interest

There are no conflicts to declare.

Data availability

The data supporting this article have been included in the article or as part of the supplementary information (SI). Supplementary information: details of the synthesis procedure, modelling, spectroscopic and electrochemical characterizations, XPS, DFT, and performance comparison tables. See DOI: https://doi.org/10.1039/d5cc06145h.

References

1 (*a*) S. Li, L. Shi, Y. Guo, J. Wang, D. Liu and S. Zhao, *Chem. Sci.*, 2024, **15**, 11188–11228; (*b*) Z. Pei, H. Zhang, Y. Guo, D. Luan, X. Gu and X. W. Lou, *Adv. Mater.*, 2024, **36**, 2306047; (*c*) Z.-P. Wu, S. Zuo, R. Wu, C. Chen, X. Zhao, Y. Ren, X. T. Xiao, J. Zhang, J. Ruiz-Martinez, Z. P. Liu and H. Zhang, *J. Am. Chem. Soc.*, 2025, **147**, 36763–36773; (*d*) X. F. Lu, S. L. Zhang, E. Shangguan, P. Zhang, S. Gao and X. W. Lou, *Adv. Sci.*, 2020, **7**, 2001178.
2 (*a*) A. P. Côté, A. I. Benin, N. W. Ockwig, M. O'Keeffe, A. J. Matzger and O. M. Yaghi, *Science*, 2005, **310**, 1166–1170; (*b*) K. Geng, T. He, R. Liu, S. Dalapati, K. T. Tan, Z. Li, S. Tao, Y. Gong, Q. Jiang and D. L. Jiang, *Chem. Rev.*, 2020, **120**, 8814–8933; X. T. Ren, M. Y. Wen, X. B. Hou, J. J. Sun, F. Bai and Y. S. Li, *Chem. Commun.*, 2024, **60**, 4423–4426.
3 R. Cheng, B. Ran, X. Zhang, Y. Han, X. Shao, H. Li and C. Fu, *Adv. Funct. Mater.*, 2024, **34**, 2406717.
4 (*a*) B. Li, S. Y. Zhang, B. Wang, Z. J. Xia, C. Tang and Q. Zhang, *Energy Environ. Sci.*, 2018, **11**, 1723–1729; (*b*) S. Bhunia, A. Peña-Duarte, H. Li, H. Li, M. F. Sanad, P. Saha, M. A. Addicoat, K. Sasaki, T. A. Strom, M. J. Yacaman, C. R. Cabrera, S. Bhattacharya, J. Bredas and L. Echegoyen, *ACS Nano*, 2023, **17**, 3492–3505.
5 H. Zhang, Z. Qu, H. Tang, X. Wang, R. Koehler, M. Yu, C. Gerhard, Y. Yin, M. Zhu, K. Zhang and O. G. Schmidt, *ACS Energy Lett.*, 2021, **6**, 2491–2498.
6 (*a*) Y. Tian, X. Hui, K. Wang, Y. Yuan, H. Chen, K. T. Bang, R. Tao, R. Wang, D. Shin, Y. Lan, Z. Xu and Y. Kim, *Angew. Chem., Int. Ed.*, 2024, **137**, e202419257; (*b*) Q. Cao, L. Wan, Z. Xu, W. Kuang, H. Liu, X. Zhang, W. Zhang, Y. Lu, Y. Yao, B. Wang and K. Liu, *Adv. Mater.*, 2023, **35**, 2210550.
7 (*a*) C. Liu, F. Liu, H. Li, J. Chen, J. Fei, Z. Yu, Z. Yuan, C. Wang, H. Zheng, Z. Liu, M. Xu, G. Henkelman, L. Wei and Y. Chen, *ACS Nano*, 2021, **15**, 3309–3319; (*b*) D. Li, C. Li, L. Zhang, H. Li, L. Zhu, D. Yang, Q. Fang, S. Qiu and X. Yao, *J. Am. Chem. Soc.*, 2020, **142**, 8104–8108.
8 H. Liu, X. Zheng, J. Xu, X. Jia, M. Chao, D. Wang and Y. Zhao, *ACS Appl. Mater. Interfaces*, 2023, **15**, 16794–16800.
9 B. N. Nandre, S. Halder, S. Dalapati, A. Bhaumik and C. Chakraborty, *Sol. Energy Mater. Sol. Cells*, 2026, **295**, 113979.
10 B. K. Nandre, S. Halder and C. Chakraborty, *Chem. – Asian J.*, 2025, **20**, e202401460.
11 S. Ruidas, A. Das, S. Kumar, S. Dalapati, U. Manna and A. Bhaumik, *Angew. Chem., Int. Ed.*, 2022, **61**, e202210507.
12 Z. M. Wang, Q. Song, C. He, P. Y. Feng, L. Zhao and C. Y. Duan, *Chem. Commun.*, 2024, **60**, 4793–4796.
13 R. Cheng, K. Li, Z. Li, M. Jiang, F. Wang, Z. Yang, T. Zhao, P. Meng and C. Fu, *J. Power Sources*, 2023, **556**, 232476.
14 I. Fareed, M. D. Khan, M. Firdous, T. Maqsood, M. U. H. Farooq, M. Tahir, F. K. Butt, J. J. Zou and S. Du, *Adv. Sci.*, 2025, **12**, e09902.
15 R. Brandiele, A. Guadagnini, M. Parnigotto, F. Pini, V. Coviello, D. Badocco, P. Pastore, G. A. Rizzi, A. Vittadini, D. Forrer, V. Amendola and C. Durante, *J. Energy Chem.*, 2024, **92**, 508.
16 A. K. Pradhan, S. Halder, S. G. Palani and C. Chakraborty, *J. Power Sources*, 2025, **659**, 238425.